Thermal tomography utilizing truncated Fourier series approximation of the heat diffusion equation

J.M. Toivanen[a,*], T. Tarvainen[a,b], J.M.J. Huttunen[a], T. Savolainen[a], A. Pulkkinen[a], H.R.B. Orlande[c], J.P. Kaipio[a,d], V. Kolehmainen[a]

[a] *Department of Applied Physics, University of Eastern Finland, P.O. Box 1627, 70211 Kuopio, Finland*
[b] *Department of Computer Science, University College London, Gower Street, London WC1E 6BT, UK*
[c] *Department of Mechanical Engineering, Politecnica/COPPE, Federal Univesity of Rio de Janeiro, Cid. Universitaria, Cx. Postal 68503, 21941-972 Rio de Janeiro, Brazil*
[d] *Department of Mathematics, University of Auckland, Private Bag 92019, Auckland Mail Centre, Auckland 1142, New Zealand*

Abstract

In a thermal tomography measurement setup, a physical body is sequentially heated at different source locations and temperature evolutions are measured at several measurement locations on the surface of the body. Based on these transient measurements, the thermal conductivity, the volumetric heat capacity and the surface heat transfer coefficient of the body are estimated as spatially distributed parameters, typically by minimizing a modified data misfit functional between the measured data and the data computed with the estimated thermal parameters. In thermal tomography, heat transfer is modeled with the time-dependent heat diffusion equation for which direct time domain solving is computationally expensive. In this paper, the computations of thermal tomography are sped up by utilizing a truncated Fourier series approximation approach. In this approach, a frequency domain equivalent of the time domain heat diffusion equation is solved at multiple frequencies and the solutions are used to obtain a truncated Fourier series approximation for the solution and the Jacobian of the time domain heat transfer problem. The feasibility of the approximation is tested with simulated and experimental measurement data. When compared to a previously used time domain approach, it is shown to lead to a significant reduction of computation time in image reconstruction with no significant loss of reconstruction accuracy.

Keywords: Thermal tomography, Truncated Fourier series approximation, Inverse problem, Thermal conductivity, Volumetric heat capacity, Surface heat transfer coefficient, Non-destructive testing

1. Introduction

Thermal tomography is an emerging non-destructive imaging technique which aims at recovery of three-dimensional images of the thermal conductivity and heat capacity of a physical body from non-invasive temperature measurements made on the surface of the body [1–11]. In the measurement process, the body is heated at a source location and temperature evolutions are measured at multiple measurement locations on the surface. The same process is then repeated for a number of source locations. Finally the measured temperature evolutions are used to estimate the unknown thermal conductivity and heat capacity as spatially distributed parameters which can be visualized as three-dimensional images. Potential applications of thermal tomography include characterization of thermal properties and non-destructive testing, such as detecting and locating air bubbles, cracks, porosity and other defects that alter thermal properties of materials.

The heatings and the temperature measurements can be chosen to be contact or non-contact based depending on the application. When physical contact with the body is practical, it is possible to use contact heaters, such as heating resistors, and contact temperature sensors, such as thermocouples or thermistors. Alternatively, if no contact is desired, inductive or laser heatings as well as thermography (IR-camera) measurements can be used.

Solving the thermal conductivity and the heat capacity of the body as spatially distributed parameters given the boundary measurements of heat transfer is a non-linear and ill-posed inverse boundary value problem which is unstable with respect to measurement and modeling errors. In this paper, this inverse problem is considered in the framework of Bayesian inversion [12, 13].

Thermal tomography has been studied with simulations in [1–10]. The spatially distributed thermal conductivity of a two-dimensional (2D) body was estimated using simulated steady state measurements in [1] and that of three-dimensional (3D) bodies with known heat capacities using simulated transient state measurements in [2, 3]. The estimation of either the spatially distributed thermal

*Corresponding author. Tel.: +358 40 355 2272; E-mail address: Jussi.Toivanen@uef.fi (J.M. Toivanen).

conductivity or the spatially distributed heat capacity of a 2D body while the other parameter was assumed known was studied in [4]. In [5], defects in 2D bodies were located using discrete variable thermal tomography, an approach where each pixel of the resulting image is allowed one of two possible sets of thermal properties, that is, the *a priori* known values of the intact or the defect area. Furthermore, 2D spatially distributed and time dependent thermal conductivity was estimated in [6] while the heat capacity was assumed known. The thermal conductivity and the shape of an inclusion were estimated in [7] using simulated steady state measurements with the thermal properties of the body otherwise known. More complexity was added in [8, 9] when both the thermal conductivity and the heat capacity of 2D bodies were treated as unknowns and were estimated from transient boundary measurements.

In [9], it was demonstrated using simulated data from a 2D body that simultaneous estimation of spatially distributed thermal conductivity and volumetric heat capacity from transient boundary data is feasible when the boundary heat flux between the body and the surrounding medium is known. However, in practice such a measurement setup would not always be feasible as it requires the body to be insulated from the surrounding medium. In [10], the computational methods of [9] were extended towards a more practical setup of imaging bodies where the boundary heat flux between the body and the surrounding medium is not known (i.e. the body is not insulated). This was implemented by treating the surface heat transfer coefficient as a spatially distributed parameter at the surface, and estimating it simultaneously with the spatially distributed thermal conductivity and volumetric heat capacity.

In [11], the feasibility of thermal tomography was tested using experimental measurement data with computational methods modified from those of [10]. The data was measured from a mortar body using a prototype thermal tomography measurement device which uses heater resistors for heating and thermistors for temperature measurements at the surface of the body. The shape and location of an air cavity were clearly visible in the estimates of thermal conductivity and heat capacity, implying that thermal tomography with experimental measurement data is feasible.

We note that infrared thermography techniques [14–23] are somewhat related to thermal tomography, the main difference being that infrared thermography techniques are designed to detect defects that are located relatively close to the surface of the body, whereas thermal tomography aims at locating defects within the whole volume of the body and at giving quantitative solutions of the thermal conductivity and the heat capacity as well.

The forward model of thermal tomography which is used to model the time evolution of temperature inside the body is the time-dependent heat diffusion equation. In [11], the computational approach to solve the semi-discrete finite element approximation of this model and the related Jacobians was based on an implicit Euler scheme which makes estimating the thermal parameters time consuming. In this paper, we propose a truncated Fourier series approximation approach to reduce the computational cost of thermal tomography. In the proposed approach, the time-domain forward solution and Jacobians are approximated by a truncated Fourier series which is based on a small number of solutions of the frequency domain heat diffusion equation. The feasibility of the approach is evaluated with simulated and experimental measurement data by comparing the forward model solutions and the estimates of the thermal parameters to those obtained with the time domain approach of [11]. Previously, a similar Fourier series approximation for the solution of a time-dependent partial differential equation has been utilized for the solution of the time domain radiative transfer equation in [24]. In [25], a parallelized Fourier series truncated diffusion approximation was used to accelerate diffuse fluorescence tomography.

The rest of the paper is organized as follows. The modeling of heat transfer is discussed in Section 2 and the numerical implementation of the heat transfer modeling in Section 3. The estimation of the thermal parameters is discussed in Section 4. The measurement setup and parameter choices are discussed in Section 5 and the results using simulated and experimental measurement data are given and discussed in Section 6. Section 7 gives the conclusions.

2. Modeling of heat transfer

2.1. Time domain heat transfer

Let $\Omega \subset \mathbb{R}^3$ model the domain of the target, i.e. the domain of the body under investigation, with boundary $\partial\Omega$, let $\Xi_k \subset \partial\Omega$ $(k = 1, \ldots, N_\Xi)$ be the surface patches that are covered by the heater elements and $\xi_j \in \partial\Omega$ $(j = 1, \ldots, N_\xi)$ denote the locations of the point-like temperature sensors. In the measurement process, one of the heaters is turned on at a time for a time period t_{heat} and it produces a heat flux into the target at Ξ_k. This is followed by a cooling period of t_{cool} seconds before the next heater is turned on. While this is repeated for all heaters, the evolution of temperature is measured every Δt_m at all of the measurement locations for the duration of the measurement process $t_{\text{meas}} = N_\Xi(t_{\text{heat}} + t_{\text{cool}})$.

Heat transfer is modeled with the heat diffusion equation and the boundary conditions

$$c(x)\frac{\partial T(x,t)}{\partial t} = \nabla \cdot (\kappa(x)\nabla T(x,t)), \quad x \in \Omega \tag{1}$$

$$\kappa(x)\frac{\partial T(x,t)}{\partial \hat{n}} = q(x,t), \quad x \in \partial\Omega \tag{2}$$

$$T(x,0) = T_0 \tag{3}$$

where $c(x)$ is the volumetric heat capacity, $\kappa(x)$ is the thermal conductivity, $T(x,t)$ is the temperature, $q(x,t)$ is the heat flux, x is the position vector in Ω, t is time, $\hat{n}$ is the outward pointing unit normal of $\partial\Omega$ and T_0 is the initial temperature of the target [26].

The boundary condition modeling the heat flux at the surface of the target can be split into heat flux between the heaters and the target, and heat flux between the target and the surrounding medium. Thus

$$q(x,t) = \begin{cases} b\big(T_{\mathrm{H,k}}(t) - T(x,t)\big), & x \in \Xi_k \\ h(x)\big(T_\infty(t) - T(x,t)\big), & x \in \partial\Omega_{\mathrm{S}} \end{cases} \tag{4}$$

where $b = \kappa_b/L_b$ is the thermal contact conductance coefficient where κ_b and L_b are the thermal conductivity and the thickness of the contact layer between the heater and the target, $T_{\mathrm{H},k}(t)$ is the temperature of the heater at the surface patch Ξ_k, $h(x)$ is the surface heat transfer coefficient, $T_\infty(t)$ is the temperature of the surrounding medium and $\partial\Omega_{\mathrm{S}} = \partial\Omega \backslash \Xi_{k=1,\ldots,N_\Xi}$ is the part of the boundary that is not covered by heater elements [11].

2.2. Truncated Fourier series approximation

By using the notation $\tau(x,t) = T(x,t) - T_0$ and the Fourier transformation, the parabolic heat transfer problem (1)–(3) can be transformed into the elliptic frequency domain heat transfer problem

$$i\omega_j c(x)\tau(x,\omega_j) = \nabla\cdot(\kappa(x)\nabla\tau(x,\omega_j)), \quad x \in \Omega \tag{5}$$

with the boundary condition

$$\kappa(x)\frac{\partial\tau(x,\omega_j)}{\partial\hat{n}} = \begin{cases} b\big(\tau_{\mathrm{H,k}}(\omega_j) - \tau(x,\omega_j)\big), & x \in \Xi_k \\ h(x)\big(\tau_\infty(\omega_j) - \tau(x,\omega_j)\big), & x \in \partial\Omega_{\mathrm{S}} \end{cases} \tag{6}$$

where i is the imaginary unit and ω_j is the angular frequency. Based on the solutions $\tau(x,\omega_j)$ of the model (5)–(6), the time domain solution can, in principle, be obtained with the infinite Fourier series

$$T(x,t) = T_0 + \sum_{j=-\infty}^{\infty} \tau(x,\omega_j)\exp(i\omega_j t) \tag{7}$$

if solutions were available with all frequencies. However, in practice, solutions can be computed using only a limited number of frequencies and $T(x,t)$ is approximated using the truncated Fourier series approximation

$$T(x,t) \approx T_0 + \sum_{j=-N_\omega}^{N_\omega} \tau(x,\omega_j)\exp(i\omega_j t) \tag{8}$$

where N_ω is the number of Fourier frequencies ω_j used in the approximation.

Similar Fourier series approximations have been used for diffuse optical tomography [24] and for diffuse fluorescent tomography [25].

3. Numerical implementations

3.1. Numerical solution of the heat transfer problem

In this paper, a finite element method (FEM) is used for numerical approximation of the heat transfer problem (5)–(6). The FE-approximation can be derived similarly as for the time domain problem in [11].

The domain Ω is discretized into N_e tetrahedral elements connected at N_n vertex nodes. The solution of (5)–(6) is then approximated as

$$\tau(x,\omega) \approx \sum_{j=1}^{N_n} a_j(\omega)\varphi_j(x) \ \in Q_h \tag{9}$$

where $a_j(\omega)$ are the values of $\tau(x,\omega)$ at the nodes of the FE mesh, $\varphi_j(x)$ are piecewise linear nodal basis functions and the space $Q_h = \mathrm{span}\{\varphi_{\mathrm{j}}\}$. To have reasonable accuracy for the FE-approximation without making the computations too expensive, the computational mesh of the temperatures is often chosen to be denser near the source locations than elsewhere.

The unknowns $\kappa(x)$, $c(x)$ and $h(x)$ are approximated in a uniform mesh of N_{ep} elements and N_{np} nodes. This gives the approximations

$$\kappa(x) \approx \sum_{p=1}^{N_{np}} \kappa_p\psi_p(x) \tag{10}$$

$$c(x) \approx \sum_{p=1}^{N_{np}} c_p\psi_p(x) \tag{11}$$

$$h(x) \approx \sum_{p\in\partial\Omega_{\mathrm{S}}} h_p\psi_p(x)\big|_{\partial\Omega_{\mathrm{S}}} \tag{12}$$

where $\psi_p(x)$ are piecewise linear nodal basis functions, κ_p, c_p, and h_p are the values of thermal conductivity, volumetric heat capacity and surface heat transfer coefficient at node p. In Equation (12), $p \in \partial\Omega_{\mathrm{S}}$ are the N_{hp} indices of the basis functions on $\partial\Omega_{\mathrm{S}}$.

Using the approximations (9)–(12) and the Galerkin approach leads to the linear system

$$(i\omega_j M + G + F + W)\alpha = V + Q, \tag{13}$$

where

$$\alpha := \alpha(\omega_j) = [a_1(\omega_j), \ldots, a_{N_n}(\omega_j)]^{\mathrm{T}}$$

and the elements of the matrices and vectors are

$$M_{il} = \int_\Omega \sum_{p=1}^{N_{np}} c_p\psi_p(x)\varphi_l(x)\varphi_i(x)\mathrm{dx} \tag{14}$$

$$G_{il} = \int_\Omega \sum_{p=1}^{N_{np}} \kappa_p\psi_p(x)\nabla\varphi_l(x)\cdot\nabla\varphi_i(x)\mathrm{dx} \tag{15}$$

$$F_{il} = \int_{\partial\Omega_{\mathrm{S}}} \sum_{p\in\partial\Omega_{\mathrm{S}}} h_p\psi_p(x)\varphi_l(x)\varphi_i(x)\mathrm{dS} \tag{16}$$

$$W_{il} = \sum_{k=1}^{N_\Xi} \int_{\Xi_k} b\varphi_l(x)\varphi_i(x)\mathrm{dS} \tag{17}$$

$$V_i = \sum_{k=1}^{N_\Xi} \int_{\Xi_k} b\tau_{\mathrm{H,k}}(\omega_j)\varphi_i(x)\mathrm{dS} \tag{18}$$

$$Q_i = \int_{\partial\Omega_S} \sum_{p\in\partial\Omega_S} h_p \psi_p(x) \tau_\infty(\omega_j) \varphi_i(x) \mathrm{dS} \tag{19}$$

where $i, l = 1, \ldots, N_n$.

The computed frequency domain temperatures at measurement locations are obtained with

$$\mathcal{F}(\omega_j, \kappa, c, h) = \tilde{M}\alpha(\omega_j) \tag{20}$$

where $\tilde{M}$ is a measurement operator. Now the corresponding time domain temperatures can be obtained with

$$\mathcal{F}(t, \kappa, c, h) \approx T_0 + \sum_{j=-N_\omega}^{N_\omega} \mathcal{F}(\omega_j, \kappa, c, h) \exp(i\omega_j t) \tag{21}$$

Furthermore, the connection between the measured and computed temperatures is modeled as

$$y = \mathcal{F}(t, \kappa, c, h) + e, \quad e \sim \mathcal{N}(0, \Gamma_e) \tag{22}$$

where e contains the random additive zero-mean Gaussian measurement errors with covariances defined by the covariance matrix Γ_e.

3.2. Numerical solving of the Jacobian

The Jacobian of $\mathcal{F}(t, \kappa, c, h)$ is required for solving the thermal parameters as described in the next section of this paper. In the frequency domain, the Jacobian is of the form

$$J(\omega_j) = \begin{bmatrix} J_\kappa(\omega_j) & J_c(\omega_j) & J_h(\omega_j) \end{bmatrix} \tag{23}$$

where for $\beta = \kappa, c, h$ the elements of the row vector $J_\beta(\omega_j)$ are

$$\begin{aligned} J_\beta(\omega_j)[i] &= \frac{\partial \mathcal{F}(\omega_j, \kappa, c, h)}{\partial \beta_i} \\ &= \tilde{M}\frac{\partial \alpha(\omega_j)}{\partial \beta_i}, \; i = 1, \ldots, N_p \end{aligned} \tag{24}$$

where $N_p = N_{np}$ for $\beta = \kappa, c$, and $N_p = N_{hp}$ for $\beta = h$. The partial derivatives $\partial\alpha(\omega_j)/\partial\beta_i$ are obtained by derivating (13) and by solving the so obtained equations

$$-B\frac{\partial \alpha}{\partial \kappa_k} = \frac{\partial G}{\partial \kappa_k}\alpha \tag{25}$$

$$-B\frac{\partial \alpha}{\partial c_k} = \frac{\partial M}{\partial c_k} i\omega_j \alpha \tag{26}$$

$$-B\frac{\partial \alpha}{\partial h_l} = \frac{\partial F}{\partial h_l} - \frac{\partial Q}{\partial h_l} \tag{27}$$

for $k = 1, \ldots, N_{np}$ and $l = 1, \ldots, N_{hp}$ where

$$B = (i\omega_j M + G + F + W) \tag{28}$$

The truncated Fourier series approximation of the time domain Jacobian is then obtained as

$$J(t) \approx \sum_{j=-N_\omega}^{N_\omega} J(\omega_j) \exp(i\omega_j t) \tag{29}$$

4. Estimation of thermal parameters

Following the Bayesian approach proposed in [11], the maximum a posteriori (MAP) estimates of thermal conductivity, volumetric heat capacity and surface heat transfer coefficient are obtained by minimizing

$$\begin{aligned} (\kappa, c, h)_{\mathrm{MAP}} = \arg \min_{(\kappa,c,h)>0} \Big\{ \\ \|L_e(y - \mathcal{F}(t, \kappa, c, h))\|^2 + \|L(\theta - \theta_*)\|^2 \Big\} \end{aligned} \tag{30}$$

where L_e is the Cholesky decomposition of the noise precision matrix, i.e. $L_e^{\mathrm{T}} L_e = \Gamma_e^{-1}$. Correspondingly, L is the Cholesky decomposition of the prior precision matrix, i.e. $L^{\mathrm{T}} L = \Gamma^{-1}$ and

$$\Gamma^{-1} = \begin{bmatrix} \Gamma_\kappa^{-1} & 0 & 0 \\ 0 & \Gamma_c^{-1} & 0 \\ 0 & 0 & \Gamma_h^{-1} \end{bmatrix} \tag{31}$$

The prior precision matrix is based on the smoothness prior model used in [11]. The construction of the prior was originally proposed in [27]. In (30), the vectors of thermal parameters κ, c, h and their prior means κ_*, c_* and h_* are concatenated into the column vectors

$$\theta = (\kappa;\, c;\, h) \tag{32}$$

$$\theta_* = (\kappa_*;\, c_*;\, h_*) \tag{33}$$

The minimization problem (30) can be solved using Gauss-Newton optimization. For more details, see [11].

5. Measurement setup and parameters

5.1. Experimental measurement setup and target

The measurement device, the measurement setup and the measurement parameters used in this work are the same as in [11] where the prototype thermal tomography measurement device was previously used. For heatings, the measurement device uses eight heating resistors with dimensions $0.55 \times 1 \times 0.55$ cm (width×height×thickness) which are attached to the test target with epoxy glue. For making measurements, eight negative temperature coefficient (NTC) thermistors are attached to the test target. The device also measures the temperature of the surrounding air using a NTC thermistor which can be placed away from the test target and the heaters. The measurement device is shown in Figure 1.

The target used in this work was a cylinder with diameter of 7.1 cm and height of 2.1 cm. It was made from a mortar mass with 0.18 l/kg water to mortar ratio. The mass was moist cured for 14 days in a mould containing a smaller cylinder to create an air filled hole to the final target. The hole had diameter of 3.1 cm and it went through the target from the top surface to the bottom so that the distance between the closest point of the hole and the mantle of the target was 1.0 cm. The target can

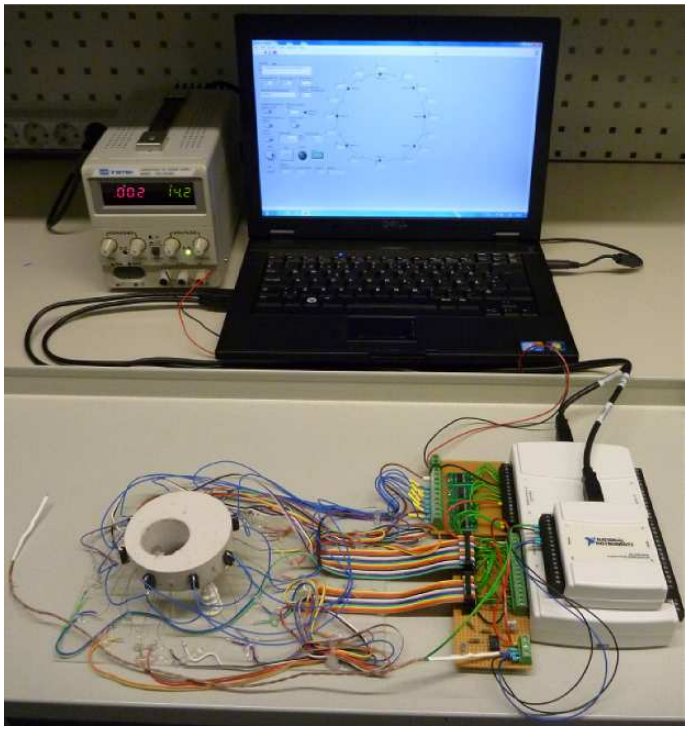

Figure 1: The measurement device and the test target without the insulating discs. The voltage source of the heater resistors is located in the top left corner, the laptop with the measurement software next to it and the measurement electronics in the bottom right corner next to the target in the bottom left corner. Picture from [11].

be seen in Figure 1. Figure 2 shows the locations of the heaters and the measurement sensors on the mantle of the target.

In the measurement setup, the target was sandwiched between two insulating discs made of expanded polystyrene, as shown in Figure 3. With this setup, the values of the surface heat transfer coefficient on the top and bottom surfaces of the target were low in comparison to the values on the mantle.

In the measurement process, the heaters were one at a time turned on for $t_{\text{heat}} = 180$ s and the cooling period, when no heater was active, was $t_{\text{cool}} = 720$ s. Temperatures were measured for $t_{\text{meas}} = 7200$ s every $\Delta t_m = 2$ s, resulting in a measurement vector $y \in \mathbb{R}^{m_{\text{meas}}}$ where the number of measurements $m_{\text{meas}} = 28{,}000$.

5.2. Simulation measurement setup and target

To verify the numerical approach of Section 3, in addition to the experimental measurement data based tests, the approach was also tested with simulations.

The geometry of the simulation test target was chosen to match that of the actual target described in Section 5.1. Thermal conductivity for the intact part was set to 0.6 W/(m K), volumetric heat capacity to $1.0{\cdot}10^6$ J/(m^{3}K) and surface heat transfer coefficient to 5 W/(m^{2}K) for the mantle and to 0 W/(m^{2}K) for the top and bottom surfaces.

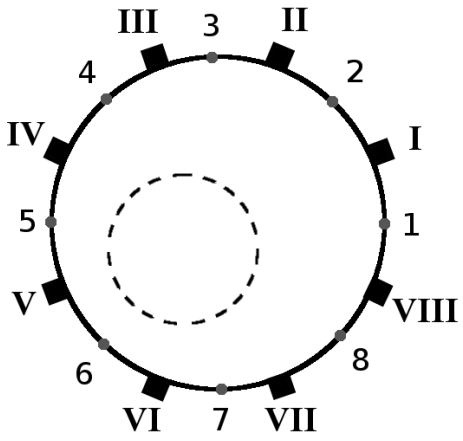

Figure 2: Schematic showing the locations of the measurement sensors (Arabic numerals) and the heaters (Roman numerals). The location of the cavity is shown with a dashed line. Picture from [11].

For the volume corresponding to the cavity, thermal conductivity was set to 0.03 W/(m K) and volumetric heat capacity to 1000 J/(m^3 K). The simulation test target can be seen in the leftmost column in Figure 6.

To simulate the data, the heat transfer problem (1)–(3) was solved using the time domain approach of [11]. This involved solving the heat transfer problem with a finite element method and solving the semidiscrete problem with an implicit Euler iteration. A mesh of 2659 nodes and 11858 elements was used for the computing of the simulated measurement data.

A noisy realization of the simulated data was obtained by adding Gaussian zero mean random noise with standard deviation $\sigma_e = 0.1$ °C to the simulated noiseless data. Noise with the same standard deviation was also added to the simulated noiseless heater temperatures and the simulated noiseless temperature of the surrounding medium.

The heat flux from the heaters into the target was modeled by Equation (4) with the thermal contact conductance coefficient set to $b = 1000$ W/(m^{2}K) [11].

5.3. Discretization and parameters

The number of elements, nodes and boundary nodes in the finite element meshes used for the forward solution and the parameters (κ, c, h) are listed in Table 1. Note that the mesh that was used for computation of the simulated measurement data was more dense than the ones used for the solution of the inverse problem to avoid committing an inverse crime[1].

The prior means and standard deviations of the thermal parameters used in the prior model were chosen as follows. As the actual thermal property values of the mortar part of the target were not known, the prior means

[1] Using the same mesh for data generation and estimation of the unknown parameters can give misleadingly good results [12, 28].

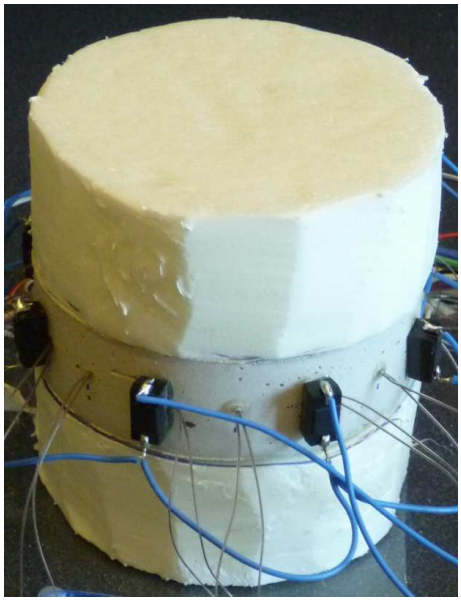

Figure 3: The target sandwiched between two insulating discs made of expanded polystyrene. Picture from [11].

Table 1: The number of elements, nodes and boundary nodes in the tetrahedral FE meshes for the discretization of the temperatures (N_e, N_n and N_b) and the parameters (N_{ep}, N_{np} and N_{bp}).

elements	nodes	boundary nodes
$N_e = 6834$	$N_n = 1614$	$N_b = 892$
$N_{ep} = 2009$	$N_{np} = 502$	$N_{bp} = 306$

for the thermal conductivity and the volumetric heat capacity were chosen to match the best fitting spatially constant values which were obtained as in [11] by doing a non-linear least squares fit to the measurement data. This gave $\kappa_* = 0.51$ W/(m K) and $c_* = 0.94 \cdot 10^6$ J/(m^{3}K) for the simulation case and $\kappa_* = 0.92$ W/(m K) and $c_* = 1.49 \cdot 10^6$ J/(m^{3}K) for the experimental data case. For the surface heat transfer coefficient the same prior means were used in both cases, $h_* = 0$ W/(m^{2}K) for the insulated top and bottom surfaces and $h_* = 5$ W/(m^{2}K) for the mantle. In construction of the prior precision matrices, the spatial correlation of the parameters was set by dictating that at a distance of 1.8 cm (1/4 of the diameter of the target) the covariance of two values of the same thermal parameter has decayed to a value matching 1 % of the variance. The variances were chosen to be $0.035 f_*$ where $f_* = \kappa_*$, c_*, h_* (for h_*, the prior mean of the mantle was used). For more details on construction of the precision matrices, see [11].

Measurement errors were assumed to be independent and identically distributed with standard deviation $\sigma_e = 0.1$ °C, giving the precision matrix $\Gamma_e^{-1} = \sigma_e^{-2} I$ where the identity matrix $I \in \mathbb{R}^{m_{\text{meas}} \times m_{\text{meas}}}$ where m_{meas} is the number of measurements.

The frequencies used in the truncated Fourier series approximation were chosen as follows. Data was computed for multiple targets using different equally spaced sets of frequencies. That frequency domain measurement data was transformed to time domain and compared to measurements computed with the time domain approach by computing L_2-norms of the differences. To get suitably small differences, the frequencies used in the truncated Fourier series approximation were chosen to be

$$\omega_k = \frac{F_s}{2} \frac{k}{2549} 2\pi, \;\; k = 0, \ldots, m_f - 1 \tag{34}$$

where $F_s = 1/\Delta t$ is the sampling frequency, $\Delta t = 2$ s and m_f is the number of frequencies used in the approximation and in the tests of this paper ranges from 10 to 400.

6. Results and discussion

6.1. Comparison of computed temperatures

In this section, computed temperatures $\mathcal{F}(t, \kappa, c, h)$ computed with the proposed truncated Fourier series approximation approach are compared to temperatures computed with the time domain approach of [11]. This reference approach uses an implicit Euler method with a computational time step of 1 s. Using a longer time step would cause significant errors to the computed temperatures.

The computation time of solving the temperatures using the proposed approach and speedups gained in comparison to doing the computations in the time domain are shown at the top of Figure 4. The computation times for different numbers of frequencies are shown with a dashed line and the speedups gained with a solid line. The computation time for the time domain solution, which was 26.8 s, is shown with a dashed black line.

The differences of the solutions computed with the two approaches are shown in the bottom of Figure 4 as root mean square deviations (RMSD), i.e. as sample standard deviations of the differences between the solving approaches, for different numbers of frequencies.

$$RMSD = \sqrt{\frac{\sum_{i=1}^{m_{\text{meas}}} \left(y_i^{\omega} - y_i^{\text{REF}} \right)^2}{m_{\text{meas}}}} \tag{35}$$

where y^{ω} is data computed with the proposed approach and y^{REF} is data computed with the time domain approach. For reference, the figure shows with dashed lines three different noise levels; black: $\sigma_e = 0.1$°C is the noise level used in [11], gray: $\sigma_e = 0.05$°C, and light gray: $\sigma_e = 0.01$°C.

Examining Figure 4 shows that using as few as 50 frequencies is enough to obtain a RMSD that is significantly smaller than the assumed standard deviation of the measurement errors (black dashed line). With 50 frequencies, the measurements are obtained 11.5 times faster than with the time domain approach.

The computation times of one Jacobian matrix and speedups gained when using the proposed approach instead of the time domain approach are shown in Figure 5.

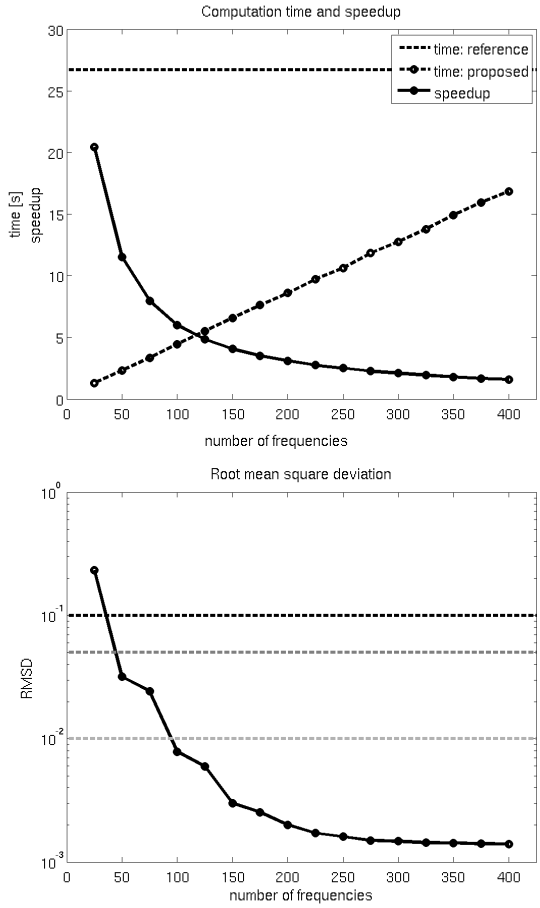

Figure 4: Comparison of single forward solutions. Top: Computation times of the proposed approach (dashed line with dots) and speedups gained by using the proposed approach (solid line with dots) instead of the reference time domain approach (computation time shown with dashed black line). Bottom: Differences between the temperatures computed with the proposed approach and temperatures computed with the time domain approach shown as the root mean square deviation. Also shown are some standard deviations of the measurement errors: $\sigma_e = 0.1$, 0.05 and 0.01°C (dashed lines).

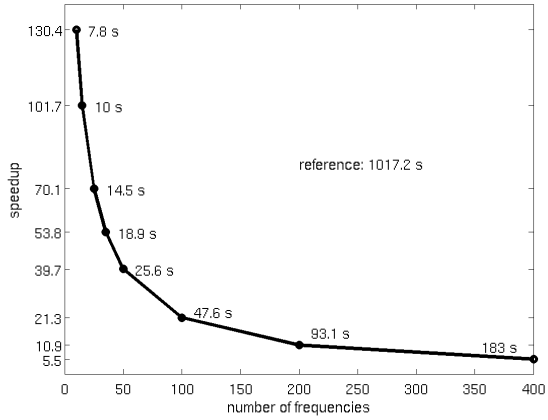

Figure 5: Speedups (line with dots) gained when computing one Jacobian matrix using the proposed approach instead of the reference time domain approach. Computation times of the proposed approach are shown next to the corresponding speedup markers.

For example with 50, 100 and 200 frequencies, the computations are 39.7, 21.3 and 10.9 times faster than in the time domain. The time domain computation of the Jacobian matrix took 1017 s and it is the main computational bottleneck of thermal tomography when employing the full time domain forward solver. This is especially true when using even denser computational meshes. With the proposed approach, the Jacobian computations are drastically faster and it is possible to choose a balance between accuracy and computational speed.

6.2. Comparison of reconstructed images

In this section, images obtained using the proposed truncated Fourier series approach are compared to those computed with the previously used time domain approach of [11]. Comparison is done first between simulation based results and then between results obtained with laboratory measurement data. The reference images obtained with the time domain approach are denoted with REF and the images obtained with the proposed truncated Fourier series approximation approach are denoted with APP.

Figure 6 shows a comparison of simulation based REF images and APP images computed with different numbers of frequencies. It can be seen that using fewer than 50 frequencies causes the APP images to deviate from the REF images. In this example case, using less than 25 frequencies makes the APP images to be of questionable usability, this is true especially for the images of volumetric heat capacity. Computing the APP images with 50 frequencies took 344 s and the REF images took 3570 s to compute.

Using experimental measurement data with the time domain approach and the proposed approach results in images shown in Figure 7. Even the APP images computed with only 25 frequencies indicate the location of the air cavity with similar accuracy as the REF images, and the computation time for the APP images was only 227 s compared to the 4290 s of the REF images.

The images computed with 10 frequencies took slightly longer to compute than the images with 25 frequencies because the errors caused by such a rough approximation made the minimization problem converge more slowly, requiring more iterations than with more frequencies.

Comparing the images computed with only 10 frequencies in the simulation and experimental cases (rightmost columns of Figures 6 and 7) reveals that the errors caused by using too few frequencies are very distinct. This suggests that it would be possible to use the Bayesian approximation error approach [12, 28] to compensate for the modeling errors caused by implementing a truncated Fourier series approach with a low number of frequencies.

For further speeding up, the proposed truncated Fourier series approximation approach can be easily parallelized as the computations of temperatures and Jacobians for dif-

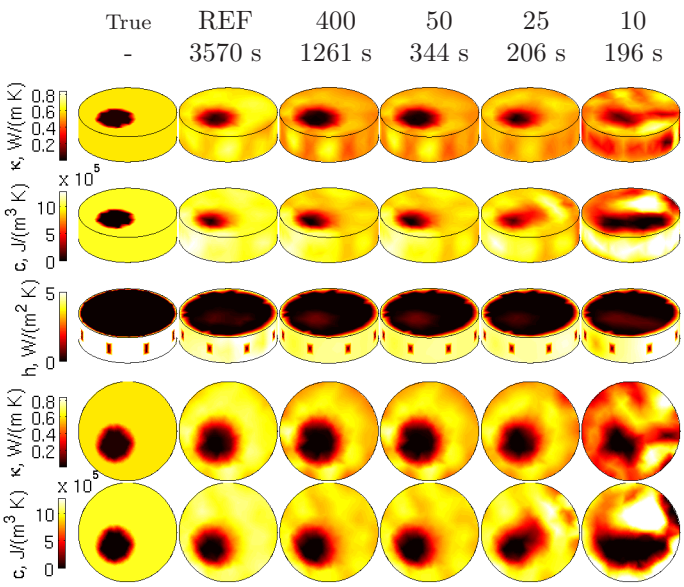

Figure 6: Estimates with simulated data. From left to right: true, REF, APP with 400, 50, 25 and 10 frequencies. From top to bottom: thermal conductivity, volumetric heat capacity and surface heat transfer coefficient in perspective view, then slices from the middles of the thermal conductivity and the volumetric heat capacity. The numbers of frequencies used in the truncated Fourier series approximation approach and the computation times for both approaches are shown above the images.

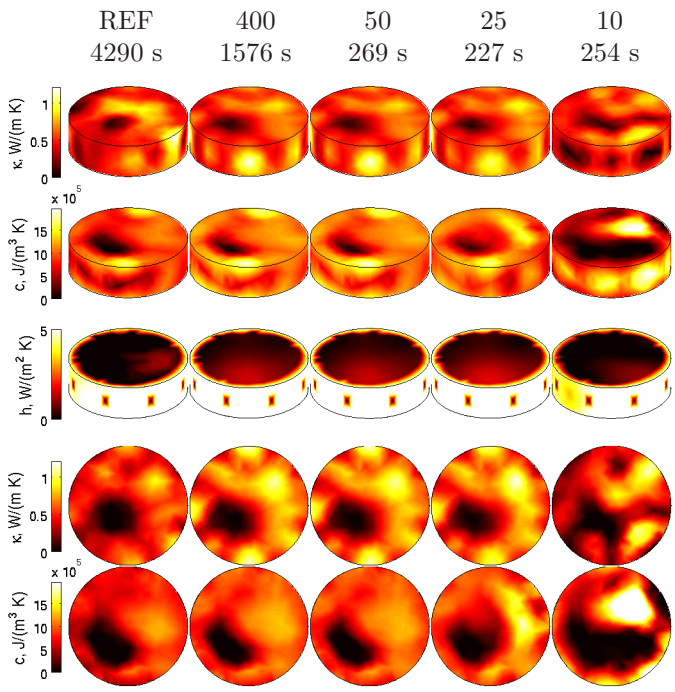

Figure 7: Estimates with experimental data. From left to right: REF, APP with 400, 50, 25 and 10 frequencies. From top to bottom: thermal conductivity, volumetric heat capacity and surface heat transfer coefficient in perspective view, then slices from the middle of the thermal conductivity and the volumetric heat capacity. The numbers of frequencies used in the truncated Fourier series approximation approach and the computation times for both approaches are shown above the images.

ferent frequencies are not dependent of each other.

7. Conclusions

A truncated Fourier series approximation approach was used to speed up the computations of thermal tomography. The time domain heat transfer problem was transformed into frequency domain and the solution of the time domain problem was approximated with a truncated Fourier series approximation using a number of frequency domain solutions. In addition to computing the measurement data without a significant loss of accuracy and faster than the implicit Euler based time domain approach of [11], also the Jacobian matrix computations were significantly sped up by doing the computations in the frequency domain. Estimates of thermal parameters with both simulated and experimental data were comparable to those computed using the computationally slower time domain approach.

Acknowledgments

This work was supported by the Academy of Finland (Projects 136220, 272803, 286247, 250215 Finnish Centre of Excellence in Inverse Problems Research), the Magnus Ehrnrooth Foundation and the Finnish Cultural Foundation. We would like to thank Asko Hänninen for helping in building the prototype measurement device and for writing the measurement software.

References

[1] M. Jones, A. Tezuka, Y. Yamada, Thermal tomographic detection of inhomogeneities, Journal of Heat Transfer 117 (1995) 969.

[2] V. Bakirov, R. Kline, Recent advances in thermal tomography, in: AIP Conference Proceedings, Vol. 760, 2005, p. 875.

[3] H. Erturk, Evaluation of image reconstruction algorithms for non-destructive characterization of thermal interfaces, International Journal of Thermal Sciences 50 (2011) 906–917.

[4] R. Kline, W. Winfree, V. Bakirov, A new approach to thermal tomography, in: AIP Conference Proceedings, Vol. 657, 2003, p. 682.

[5] V. Bakirov, R. Kline, W. Winfree, Discrete variable thermal tomography, in: AIP Conference Proceedings, Vol. 700, 2004, p. 469.

[6] C. Huang, S. Chin, A two-dimensional inverse problem in imaging the thermal conductivity of a non-homogeneous medium, International Journal of Heat and Mass Transfer 43 (22) (2000) 4061–4071.

[7] M. Ardakani, M. Khodadad, Identification of thermal conductivity and the shape of an inclusion using the boundary elements method and the particle swarm optimization algorithm, Inverse Problems in Science and Engineering 17 (7) (2009) 855–870.

[8] V. Bakirov, R. Kline, W. Winfree, Multiparameter thermal tomography, in: AIP Conference Proceedings, Vol. 700, 2004, p. 461.

[9] V. Kolehmainen, J. Kaipio, H. Orlande, Reconstruction of thermal conductivity and heat capacity using a tomographic approach, International Journal of Heat and Mass Transfer 50 (25-26) (2007) 5150–5160.

[10] J. Toivanen, V. Kolehmainen, T. Tarvainen, H. Orlande, J. Kai-

pio, Simultaneous estimation of spatially distributed thermal conductivity, heat capacity and surface heat transfer coefficient in thermal tomography, International Journal of Heat and Mass Transfer 55 (25-26) (2012) 7958–7968.

[11] J. Toivanen, T. Tarvainen, J. Huttunen, T. Savolainen, H. Orlande, J. Kaipio, V. Kolehmainen, 3d thermal tomography with experimental measurement data, International Journal of Heat and Mass Transfer 78 (2014) 1126 – 1134.

[12] J. Kaipio, E. Somersalo, Statistical and Computational Inverse Problems, Springer Science+Business Media, Inc., 2005.

[13] J. Kaipio, C. Fox, The Bayesian framework for inverse problems in heat transfer, Heat Transfer Engineering 32 (9) (2011) 718–753.

[14] K. Chatterjee, S. Tuli, S. G. Pickering, D. P. Almond, A comparison of the pulsed, lock-in and frequency modulated thermography nondestructive evaluation techniques, Nondestructive Testing & Evaluation International 44 (7) (2011) 655–667.

[15] D. Titman, Applications of thermography in non-destructive testing of structures, Nondestructive Testing & Evaluation International 34 (2) (2001) 149–154.

[16] O. Wysocka-Fotek, W. Oliferuk, M. Maj, Reconstruction of size and depth of simulated defects in austenitic steel plate using pulsed infrared thermography, Infrared Physics & Technology 55 (4) (2012) 363–367.

[17] Y. He, M. Pan, F. Luo, Defect characterisation based on heat diffusion using induction thermography testing, Review of Scientific Instruments 83 (10) (2012) 104702.

[18] M. A. Omar, Y. Zhou, A quantitative review of three flash thermography processing routines, Infrared Physics & Technology 51 (4) (2008) 300–306.

[19] D. L. Balageas, Defense and illustration of time-resolved pulsed thermography for NDE, Quantitative InfraRed Thermography Journal 9 (1) (2012) 3–32.

[20] S. Marinetti, V. Vavilov, IR thermographic detection and characterization of hidden corrosion in metals: General analysis, Corrosion Science 52 (3) (2010) 865–872.

[21] V. Vavilov, D. Nesteruk, V. Shiryaev, A. Ivanov, W. Swiderski, Thermal (infrared) tomography: Terminology, principal procedures, and application to nondestructive testing of composite materials, Russian Journal of Nondestructive Testing 46 (3) (2010) 151–161.

[22] C. Ibarra-Castanedo, X. Maldague, Pulsed phase thermography reviewed, Quantitative Infrared Thermography Journal 1 (1) (2004) 47–70.

[23] T. Sakagami, S. Kubo, Applications of pulse heating thermography and lock-in thermography to quantitative nondestructive evaluations, Infrared Physics & Technology 43 (3) (2002) 211–218.

[24] A. Pulkkinen, T. Tarvainen, Truncated fourier-series approximation of the time-domain radiative transfer equation using finite elements, Journal of Optical Society of America A 30 (3) (2013) 470–478.

[25] X. Yi, B. Wang, W. Wan, Y. Wang, Y. Zhang, H. Zhao, F. Gao, Full time-resolved diffuse fluorescence tomography accelerated with parallelized fourier-series truncated diffusion approximation, Journal of biomedical optics 20 (5) (2015) 056003–056003.

[26] A. Bejan, A. Kraus, Heat transfer handbook, Vol. 1, Wiley-Interscience, 2003.

[27] C. Lieberman, K. Willcox, O. Ghattas, Parameter and state model reduction for large-scale statistical inverse problems, SIAM Journal on Scientific Computing 32 (5) (2010) 2523–2542.

[28] J. Kaipio, E. Somersalo, Statistical inverse problems: discretization, model reduction and inverse crimes, Journal of Computational and Applied Mathematics 198 (2) (2007) 493–504.